



Cite this: *Nanoscale Adv.*, 2024, **6**, 1909

Tunable, multifunctional opto-electrical response in multilayer FePS_3 /single-layer MoS_2 van der Waals p–n heterojunctions[†]

Maria Ramos, ^{‡ab} Marcos Gadea, ^{‡ab} Samuel Mañas-Valero, ^c Carla Boix-Constant, ^c Eudomar Henríquez-Guerra, ^{ab} María A. Díaz-García, ^{ab} Eugenio Coronado ^c and M. Reyes Calvo ^{‡ab}

The combination of specific van der Waals semiconductors in vertical stacks leads to atomically sharp heterointerfaces with unique properties, offering versatility and additional functionality for thin, flexible, optoelectronic devices. In this work, we demonstrate heterostructures built from single-layer MoS_2 (n-type) and multilayer FePS_3 (p-type) as multifunctional p–n junctions where robust photoluminescent light emission and broadband electrical photo-response coexist. This is made possible by the inherent properties of the materials involved and the precise energy band alignment at their interface, which preserves the photoluminescent emission provided by the single-layer MoS_2 and confers exceptional tunability to the system. Indeed, through small changes in the applied voltage across the junction, the interplay between photoluminescence and photocurrent generation can be tuned, allowing for a precise control of the light emission of single-layer MoS_2 – from severely quenched to an order of magnitude enhancement. Additionally, the broadband photo-response of the system presents an enhanced performance under ultraviolet illumination, in contrast to other van der Waals heterostacks containing single-layer semiconductors. Furthermore, this photo-response can be adjusted by the application of an external electric field, enabling photocurrent generation under both reverse and forward bias, thereby contributing to the overall functionality and versatility of the system.

Received 19th December 2023

Accepted 26th February 2024

DOI: 10.1039/d3na01134h

rsc.li/nanoscale-advances

Introduction

Electrostatics at the interface between two semiconductors with different types of doping is at the heart of p–n junctions, the building block behind several electronic and optoelectronic devices including rectifying diodes, photodetectors, photovoltaic solar cells, and light-emitting diodes.¹ Beyond the traditional devices fabricated by epitaxial semiconductor growth, the advent of two-dimensional materials (2D materials) has raised the interest in van der Waals p–n junction prototyping.^{2–5} While these devices do not yet compete in efficiency with traditional semiconductors for typical applications, van der Waals junctions offer advantages for simplified and affordable laboratory prototyping and flexibility in the choice of materials. Depending on the properties of the specific constituents, p–n junctions

constructed from 2D materials exhibit a wide range of functionalities for different applications. These include photovoltaic solar cells,^{4,6–9} photodetection spanning from the infrared,^{10–12} to the visible,^{4,9,13} ultraviolet¹⁴ and even solar-blind^{15,16} wavelength ranges, and polarization-resolved photodetection.^{17,18} Furthermore, van der Waals p–n junctions can also operate as light-emitting devices^{19,20} or junction field-effect transistors.²¹

A key parameter in the design of p–n junctions based on 2D materials is the thickness of the constituent materials. For instance, p–n heterostacks built out of multi-layer flakes generally exhibit significantly larger electrical photo-responses compared to those containing single layers, leading to superior efficiencies in energy conversion or photodetection purposes.^{7,8} However, devices comprising single-layer, van der Waals semiconductors may offer distinct alternative advantages, thanks to the properties inherent to the 2D limit. These unique properties encompass exceptional mechanical flexibility for ultrathin optoelectronics²² and a higher tunability achieved, for instance, by electrostatic doping *via* a capacitively coupled gate voltage,^{4,5,23} than multi-layer counterparts. Furthermore, single layers of some semiconducting transition metal dichalcogenides (TMDCs) (for instance, 2H phases of MoS_2 , MoSe_2 , WS_2 , WSe_2) possess direct bandgaps and present robust excitonic emission, features absent in multi-layer flakes.^{24–26}

^aDepartamento de Física Aplicada, Universidad de Alicante, Alicante 03080, Spain.
E-mail: reyes.calvo@ua.es

^bInstituto Universitario de Materiales de Alicante (IUMA), Universidad de Alicante, Alicante 03080, Spain

^cInstituto de Ciencia Molecular (ICMol), Universidad de Valencia, Paterna 46980, Spain

† Electronic supplementary information (ESI) available. See DOI: <https://doi.org/10.1039/d3na01134h>

‡ Equal contribution.



Consequently, single-layer semiconductors can introduce new functionalities to van der Waals p–n junction devices, stemming from the interplay between electrical photo-response and photoluminescent light emission, as well as enhanced tunability through its electrical control. However, the efficient electrical photo-response of type II p–n junctions containing single-layer TMDCs typically appears accompanied by a significant quenching of their photoluminescence (PL).^{4,5,27} Consequently, the interplay between photocurrent generation and light emission remains rather unexplored in van der Waals junctions.

The combination of single-layer TMDCs with newly emerging 2D materials opens a window to explore interfaces with tailored electronic properties that could lead to desired photo-responses. While various p-type van der Waals materials with different bandgap-energy widths have been recently reported, such as WSe₂,²⁸ TeO₂ (ref. 29) or tellurene,³⁰ naturally available van der Waals, p-type materials are still less abundant than n-type ones (for a review see ref. 31). FePS₃ is a recently reported p-doped semiconductor^{32,33} that has been demonstrated to be air-stable and to exhibit a broad absorption range spanning from the infrared to the ultraviolet regimes.^{33,34} To date, FePS₃ and FePSe₃ have primarily been combined with multilayer, semiconducting, n-type TMDCs in type II heterostructures, demonstrating a broadband photo-response¹⁸ and high efficiencies for photo-detection in the ultraviolet regime,^{14,16} but lacking light emission properties. In contrast, in heterostructures made of FePS₃ with single-layer MoS₂ (FePS₃/1L-MoS₂), the photoluminescence of 1L-MoS₂ has been demonstrated to be preserved,³⁵ unlike the quenching observed in most type II, van der Waals heterostacks. This makes this system an ideal candidate to explore the interplay between photoluminescence and photocurrent generation, seeking new functionalities in p–n, van der Waals devices.

In this work, we depart from the optical characterization of FePS₃/1L-MoS₂ heterostructures and propose their integration in devices that can leverage the unique properties of each material and their interface. We found that FePS₃/1L-MoS₂ heterostructures operate as p–n photodiodes, combining a broad range photo-response with a robust photoluminescence. We explored the interplay between photocarrier dissociation and recombination and demonstrated a high electrical tunability for both photoluminescence and photocurrent generation. This allowed us to achieve a precise control of the 1L-MoS₂ light emission through just small changes in the applied bias voltage across the junction. Furthermore, we observe an enhanced responsivity of the system to wavelengths within the ultraviolet regime, a feature that is absent in other heterostructures containing single-layer TMDCs and that can be tuned through the application of a backgate voltage. Overall, we demonstrate FePS₃/1L-MoS₂ p–n devices as multifunctional, electrically-tunable p–n junctions, where both excitonic light emission and photocurrent generation can be tuned on demand.

Results and discussion

FePS₃/1L-MoS₂ van der Waals heterostructure devices were fabricated by mechanical exfoliation and deterministic transfer

of single-layer MoS₂ and multi-layer FePS₃ (40–60 nm thick, see ESI S1†) on top of respective gold contacts priorly patterned on a SiO₂/Si⁺⁺ substrate (Fig. 1a and b, see Materials and Methods). In these heterostructures, the 1L-MoS₂ lays below FePS₃ in the region where the two materials overlap (Fig. 1a).

An energy band arrangement for this heterostructure is sketched in Fig. 1c, following the one provided in ref. 35. Single-layer MoS₂ is a well-known, n-type 2D direct semiconductor with an estimated work function of ~4.8 eV³⁶ and a bandgap of 1.89 eV.² Meanwhile, FePS₃ has been reported to be a p-type indirect semiconductor with a work function around ~4.9 eV³⁵ and a bandgap of 1.23 eV³³ (Fig. 1c). Based on this, a qualitative band alignment can be constructed, assuming a conventional bulk-like Shockley model (Fig. 1d). Electrostatic equilibrium at the interface requires the transfer of 1L-MoS₂ free electron carriers to the available states in the valence band of FePS₃. The bulk-like band alignment sketched in Fig. 1d holds for the lateral junction formed along the in-plane direction of the device, with depletion regions on both sides of the junction. However, for the region where the two materials overlap, a vertical p–n junction may form. In the vertical junction, a depletion layer is not possible at the single-layer MoS₂ side,

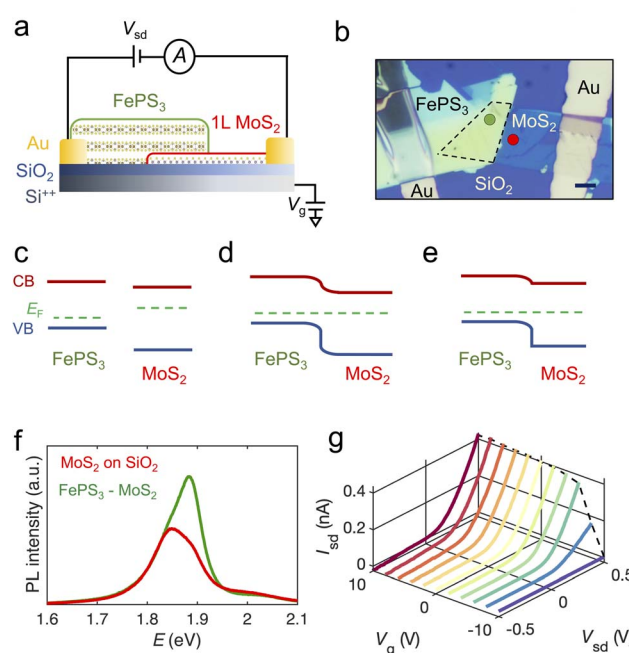


Fig. 1 (a) Sketch for a device containing a multilayer FePS₃/single-layer MoS₂ heterostructure. (b) Optical microscopy image of a heterostructure device (device A). Scale bar: 10 μ m. (c)–(e) Qualitative band alignment (c) before the two materials come into contact, (d) at the interface between the two materials in the in-plane lateral direction (lateral junction) and (e) at the interface between the two materials in the vertical direction (vertical junction). (f) PL spectra of device A taken at the single-layer MoS₂ on top of SiO₂ (red) and at the vertical heterojunction region (green), obtained at the corresponding color dots indicated in (b). PL spectra were taken using 532 nm laser excitation, with a power density of 65 μ W μ m⁻². (g) Source–drain current–voltage characteristics as a function of the applied back-gate voltage for the same device.



and the charge transfer at the interface results instead in a strong change in the doping level of the MoS_2 monolayer (Fig. 1e).

The optical transmittance of 40-to-60 nm thick FePS_3 flakes is $\sim 60\%$ for visible wavelengths,³³ which allows us to measure the PL emission of 1L- MoS_2 underneath FePS_3 . Photoluminescence (PL) spectra, acquired from device A at the marked spots on Fig. 1b at the 1L- MoS_2 on SiO_2 and at the FePS_3 /1L- MoS_2 heterostructure, respectively, are presented in Fig. 1f. In the heterostructure region, the PL emission of 1L- MoS_2 is blue shifted and narrowed when compared to that of 1L- MoS_2 directly deposited on SiO_2 . These changes in the PL emission arise from variations in the relative spectral weight of charged excitons, *versus* neutral ones. These variations have been attributed to changes in the free electron density in the 1L- MoS_2 reflecting the amount of charge transferred between FePS_3 and 1L- MoS_2 upon contact (see ref. 35 and ESI S2†). Charge transfer between 1L- MoS_2 and multilayer FePS_3 was quantified by Ramos *et al.*³⁵ as a function of the thickness of the FePS_3 layer. Here, we find a qualitatively similar behaviour, even if, in this work, 1L- MoS_2 is placed below FePS_3 , instead of above. The analysis of the PL data in Fig. S2† based on a mass action law model points also to a decrease in the charge carrier concentration of 1L- MoS_2 when integrated in FePS_3 /1L- MoS_2 heterostructures.

The optical characterization of FePS_3 /1L- MoS_2 heterostructures suggests the formation of a junction with unusual properties, in agreement with ref. 35, which could reflect in their electrical photo-response. In the following, we present the optoelectronic characterization of the FePS_3 /1L- MoS_2 heterostructure devices. Current–voltage (I – V) characteristics for the FePS_3 /1L- MoS_2 device A are presented in Fig. 1g as a function of the applied back-gate voltage (V_g). These characteristics are compatible with the formation of a potential barrier at the interface between the materials, as sketched in Fig. 1e. At zero applied gate voltage ($V_g = 0$ V), the current (I_{sd}) as a function of source–drain voltage (V_{sd}) follows the current rectifier behavior expected for a p–n diode (yellow curve in Fig. 1g). The application of a forward bias voltage ($V_{sd} > 0$ in Fig. 1g), promotes the diffusion of majority carriers across the barrier and the source–drain current grows exponentially with V_{sd} . On the other hand, the application of a reverse bias ($V_{sd} < 0$ in Fig. 1g) increases the potential barrier that blocks the passage of carriers through the barrier. Thus, the generated current (drift current) is almost negligible compared to that originated under forward bias.

Under the application of a back-gate voltage, the forward conduction of the device rapidly decreases for moderate values of $V_g < 0$, becoming negligible at $V_g \sim -10$ V. A similar behavior has been reported for 1L- MoS_2 field effect transistor devices at higher values of the applied V_g (see ref. 37 and Fig. S3†). This difference can be explained in terms of the proposed band alignment for the FePS_3 /1L- MoS_2 vertical junction in Fig. 1e. Since 1L- MoS_2 already has a reduced concentration of electrons due to their transfer to FePS_3 , a relatively small external electric field is enough to fully deplete the single-layer material and, consequently, to suppress conduction. On the contrary, the

application of a positive gate voltage ($V_g > 0$), increases the free electron density in the 1L- MoS_2 , enhancing forward conduction.

The rectification ratio (RR), defined as the ratio between the forward and reverse currents, exhibits an increase as V_g decreases, reaching a maximum value of $\text{RR} \sim 750$, at $V_g = -2$ V, for device A ($\text{RR} \sim 200$ at $V_g = -4$ V for device B) and subsequently decreases for lower values of V_g (see Fig. S4†). The maximum RR values fall within the range reported for similar heterostructures in previous studies^{9,13,38–40} (see Table S2†).

When shining light to the entire device area ($\lambda = 532$ nm), a measurable photocurrent appears at zero and reverse bias, and grows with the excitation power (Fig. 2a). This photo-response is consistent with the characteristics of photovoltaic effects, where the separation of photoexcited electron–hole pairs is driven by the interfacial built-in electric field at the p–n heterojunction. A scanning photocurrent map at $V_{sd} = 0$ V reveals that the observed photo-response mainly arises from the region of vertical contact between both semiconducting materials (Fig. 2b). This suggests that the device's response upon illumination is governed by the built-in potential at the vertical junction. The photocurrent generated at the junction interface is not spatially homogeneous, likely due to the presence of adsorbates at the interface, retained during assembly of the device, or the formation of wrinkles during the transfer process. In contrast, no measurable photocurrent is observed in the non-overlapping region of the two van der Waals materials, nor at

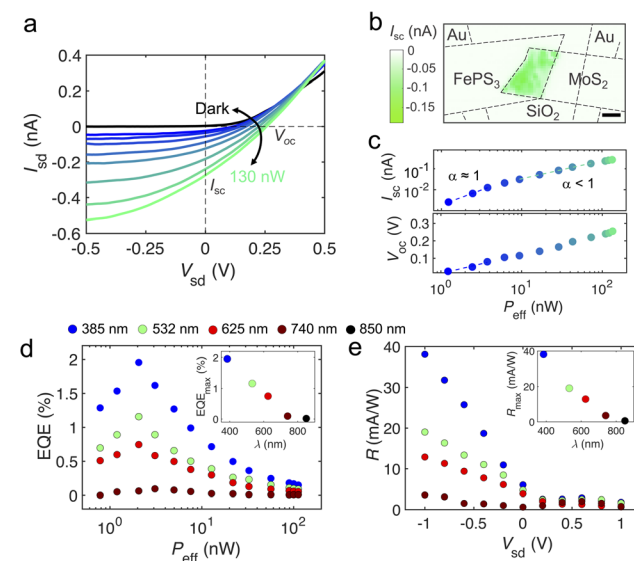


Fig. 2 (a) I_{sd} – V_{sd} characteristics of the FePS_3 /1L- MoS_2 device shown in Fig. 1b (device A) upon dark and illumination conditions at different incident, effective, optical powers. (b) Scanning photocurrent map of device A, at $V_{sd} = V_g = 0$ V, obtained with an illumination spot of ~ 1 μm diameter and $P_{\text{opt}} = 72$ nW. Scale bar: 10 μm . (c) Short-circuit current and open-circuit voltage as a function of effective power, obtained from data in panel (a). (d) External quantum efficiency (EQE) as a function of effective power for different illumination wavelengths and for $V_{sd} = 0$ V (device B). Inset: maximum EQE versus incident wavelength obtained at $V_{sd} = 0$ V. (e) Maximum responsivity R obtained at different bias (device B). Inset: maximum responsivity versus incident wavelength obtained at $V_{sd} = -1$ V.



the lateral junctions or the metal–semiconductor contact areas. This suggests a negligible contribution from drift currents or charge separation induced by Schottky barriers to the photoresponse observed under global illumination.

To further characterize the response of the $\text{FePS}_3/\text{MoS}_2$ p–n photodiode, the photocurrent at zero external bias (short-circuit current, I_{sc}) and photovoltage with no current flow (open-circuit voltage, V_{oc}) are extracted from the $I_{\text{sd}}-V_{\text{sd}}$ curves measured as a function of increasing excitation power (Fig. 2a). For small incident powers, I_{sc} displays a linear dependence on the effective power ($P_{\text{eff}} = P_{\text{opt}} \times A_{\text{device}}/A_{\text{spot}}$), whereas, for higher incident power values, it follows a power law ($I_{\text{sc}} \propto P_{\text{eff}}^{\alpha}$) with $\alpha < 1$ (Fig. 2c). This trend is commonly observed in similar systems, and it is attributed to a progressive saturation of the optical absorption of the device, due to the occupancy of photoexcited, in-gap, trapped states.⁴ Trapped carriers present larger lifetimes and low recombination probabilities, contributing to a decrease of the photocurrent generation efficiency. In the range where I_{sc} is linear with power ($P_{\text{eff}} < 4$ nW), the junction behaves according to the Shockley model, and V_{oc} follows a semi-logarithmic dependence on P_{eff} . From this dependence, we extract an ideality factor for the junction to be $n_{\text{id}} \approx 2$ (see ESI Section S5†), which describes a junction dominated by trap assisted recombination (Shockley–Read–Hall recombination mechanism).^{5,37,41}

To evaluate the performance of $\text{FePS}_3/1\text{L}-\text{MoS}_2$ photodiodes, we calculate their external quantum efficiency (EQE) and responsivity (R), which are defined as the ratios of collected charge carriers to number of incident photons, $\text{EQE} = hc \times I_{\text{ph}}/(P_{\text{eff}} \times e \times \lambda)$, and photocurrent to illumination power, $R = I_{\text{ph}}/P_{\text{eff}}$, respectively. Power conversion efficiency is also estimated in the ESI Section S6.† In Fig. 2d, EQE is presented as a function of the incident effective power at different excitation wavelengths for device B at $V_{\text{sd}} = 0$ V. For all the wavelengths, EQE increases with the incident power, reaching a maximum value before a sudden decrease at higher excitation powers. This drop in EQE with increasing power is a consequence of the optical absorption saturation inferred from the trends observed previously for I_{sc} and V_{oc} in Fig. 2c (for device A). In the visible regime, for instance at $\lambda = 532$ nm, maxima EQE of $\sim 1.2\%$ and $R \sim 5$ mA W⁻¹ are reached for device B at $P_{\text{eff}} = 2$ nW and $V_{\text{sd}} = 0$ V (being $I_{\text{ph}} \sim I_{\text{sc}}$). Similar values are obtained for other $\text{FePS}_3/1\text{L}-\text{MoS}_2$ devices (see for instance Fig. S6† for device A, showing maximum EQE $\sim 0.8\%$ and $R \sim 3.5$ mA W⁻¹ under similar conditions).

As a function of the incident wavelength (see inset of Fig. 2d), the photo-response of the heterojunction drops dramatically for $\lambda \geq 740$ nm, with nearly no EQE modulation with different incident effective powers, since these photon energies fall below the absorption threshold for single-layer MoS_2 ($E_{\text{gap}} = 1.89$ eV, $\lambda_g = 656$ nm). In contrast, the EQE of the system increases as the incident wavelength decrease (see inset in Fig. 2d). While the optical absorption of MoS_2 monolayers diminishes rapidly for excitation wavelengths below 400 nm,⁴² previous works have reported a significant photon absorption in FePS_3 flakes in the near UV regime.^{33,34} Compared to other van der Waals heterostructures, the photo-response efficiency of $\text{FePS}_3/1\text{L}-\text{MoS}_2$ is

modest for visible wavelengths (see Tables S3–S5†). However, $\text{FePS}_3/1\text{L}-\text{MoS}_2$ devices present larger EQE for more energetic wavelengths, reaching a value of $\sim 2\%$ for incident light towards the ultraviolet spectral region (Fig. 2d). Furthermore, the variation in the photo-responsivity with the applied source–drain voltage reveals a substantial increase in this efficiency for negative bias, displaying responsivity values up to $R \sim 40$ mA W⁻¹ at $V_{\text{sd}} = -1$ V for $\lambda = 385$ nm. These results indicate that $\text{FePS}_3/1\text{L}-\text{MoS}_2$ heterojunction devices can serve as efficient photodetectors when operated in the third quadrant ($V_{\text{sd}} < 0$ V), particularly for detection in the ultraviolet spectral region. This feature distinguishes them from other p–n van der Waals heterostructures containing single-layer TMDCs, which typically do not exhibit significant responsivities in the UV regime (see for example ref. 2, 4, 5, 9 and 43 and Table S5† for a comparison).

While the performance of van der Waals p–n devices containing single-layer TMDCs often tends to be smaller than those of their multilayer counterparts,⁷ they can offer distinct advantages stemming from the single-layer nature of their components. This is also the case of $\text{FePS}_3/1\text{L}-\text{MoS}_2$ heterostructures. Devices combining p-type FePS_3 or FePSe_3 with multilayer n-type TMDCs exhibit better performance than our devices (see for instance ref. 14 and 16 and Table S5† for a comparison). However, in $\text{FePS}_3/1\text{L}-\text{MoS}_2$ heterostructures, electrical photo-response appears together with a strong excitonic light emission (see Fig. 1f and 3), a characteristic which is absent in their bulk counterparts. The competition between these two phenomena cannot be easily explored in bulk, inorganic p–n junctions and has been explored for organic solar cells and semiconducting quantum well junctions.^{44,45} However, the interplay between PL and photocurrent generation remains

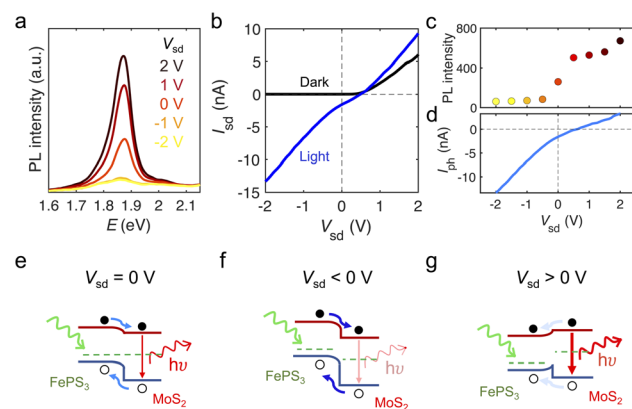


Fig. 3 (a) PL emission of single-layer MoS_2 composing the $\text{FePS}_3/1\text{L}-\text{MoS}_2$ heterojunction as a function of the applied bias voltage for a $P_{\text{eff}} = 180$ μW and $\lambda = 532$ nm (device C). Spectra are acquired at the region where the two materials overlap with an illumination spot of ~ 8 μm diameter and a collection spot of ~ 16 μm diameter. (b) $I_{\text{sd}}-V_{\text{sd}}$ characteristics under dark (black) and illumination conditions (blue) for device C under same conditions ($P_{\text{eff}} = 180$ μW , $\lambda = 532$ nm). (c) Maximum PL intensity as a function of the applied bias voltage, obtained from panel (a). (d) Photocurrent obtained from panel (b) as a function of the applied bias voltage. (e–g) Sketch showing the competition between photocurrent generation and radiative recombination mechanisms for the $\text{FePS}_3-\text{MoS}_2$ p–n heterojunction for zero (e), negative (reverse) (f) and positive (forward) (g) applied bias voltages.



rather unexplored in van der Waals p–n heterojunctions. Most heterojunctions composed of light-emitting single-layer TMDCs featuring a strong photovoltaic effect, typically present a significant PL quenching.^{4,27,46,47} In the following, we will explore the interplay between photocurrent generation and light emission in FePS₃/1L-MoS₂ van der Waals structures, taking advantage of the unusual phenomena coexistence in this system.

Our results reveal a remarkable tunability of the PL emission from single-layer MoS₂ as a function of the applied source-drain voltage (V_{sd}) across the heterojunction. In Fig. 3a, we present PL spectra acquired from an 8 μm diameter spot at the FePS₃/1L-MoS₂ vertical junction at different V_{sd} values (see Methods section for experimental details and Fig. S8† for results from a second device). A small change in bias voltage (in the order of $V_{sd} \sim 1$ V) is enough to significantly tune (suppress or enhance) the PL intensity of single-layer MoS₂ by more than ten times, a degree of tunability only reachable with large values of applied gate voltage.⁴⁸ Regarding the interplay of PL and photocurrent, when V_{sd} is set to negative values (reverse bias), we observe a significant reduction in PL intensity (Fig. 3a and c), while achieving maximum photocurrent generation (Fig. 3b and d). As V_{sd} is swept from negative to positive values, the photocurrent decreases, and the PL raises. This trend continues until V_{sd} reaches ~ 0.5 V, at which point the photocurrent approaches zero. For $V_{sd} > 0.5$ V (Fig. 3a and c), both photocurrent and PL emission increase (Fig. 3b and d).

Our findings can be qualitatively explained as follows: at $V_{sd} = 0$ V, the built-in potential at the heterointerface enables the dissociation of photoexcited electron–hole pairs, contributing to the measured photocurrent. The built-in potential generated at the FePS₃/1L-MoS₂ junction at zero bias may be small, due to the modest difference between the work function values of the two materials (~ 100 meV).³⁵ This may limit the photo-response efficiency, but, in turn, preserves the radiative recombination of excitons at the 1L-MoS₂ side, allowing for the coexistence of photocurrent and PL emission (see sketch in Fig. 3e). At $V_{sd} < 0$ V (reverse bias), the potential barrier at the interface between the two semiconducting materials increases, favoring electron–hole pair dissociation over radiative recombination (Fig. 3f). On the contrary, when applying a forward bias ($V_{sd} > 0$), the potential difference across the junction is reduced. In this situation, the contribution of photoexcited carriers to the photocurrent at the junction decreases, promoting the recombination of electron–hole pairs at 1L-MoS₂ *via* radiative pathways (Fig. 3g). Once V_{sd} surpasses the open-circuit voltage ($V_{oc} \sim 0.5$ V in our case), no photocurrent is expected to arise at the junction. In fact, negligible photocurrent is observed in photocurrent maps at $V_{sd} > 0.5$ V (see Fig. S9†). The small increase of photocurrent at positive bias in Fig. 3d is likely related to photoconductivity and photogating effects. Nonetheless, this photocurrent does not seem to directly compete with the PL emission which continues to increase with $V_{sd} > 0.5$ V.

It is worth noting that the alignment sketched for $V_{sd} > 0$ V in Fig. 3g would, in principle, allow the transfer of both electrons and holes from 1L-MoS₂ to FePS₃ and potentially enable the emergence of electroluminescence, which has been observed

for similar energy band arrangements in other van der Waals heterojunctions.^{43,49} However, the substantial increase of exciton radiative recombination suggests that the photocarrier transfer from 1L-MoS₂ to FePS₃ at positive bias must be small in our system, likely due to the momentum mismatch of MoS₂ and FePS₃ band structures.³⁵ Besides, electroluminescence would not be expected to be a leading effect in an indirect gap semiconductor such as FePS₃. The efficiency of non-radiative recombination processes, such as Auger⁵⁰ or trap-assisted recombination,^{5,37,41} might also vary with the applied bias, and could explain further details of the photocurrent and photoluminescence behaviour, for example, the saturation in the PL increase for $V_{sd} > 1$ V (see ESI S13†).

Finally, we found that the photo-response of the FePS₃/1L-MoS₂ p–n diodes can be modulated by applying a back-gate voltage (Fig. 4a and S10†). In terms of the incident power, we distinguish two different regimes for photocurrent generation as a function of V_g . First, we observed that for low excitation power ($P_{\text{eff}} \sim 10$ nW) the photocurrent – and, thus, the responsivity – at zero and reverse bias ($V_{sd} \leq 0$) increases towards positive values of V_g (Fig. 4b), as the built-in potential at the junction increases. Conversely, a negative gate voltage would lower the potential barrier at the junction and justify the decrease of photocurrent for negative values of V_g observed in Fig. 4b. It is worth noting that the modulation of the photocurrent at $V_g > 0$ is smaller in our heterostructures compared to other systems, such as BP/1L-MoS₂.⁹ This difference could be due to the higher resistance of FePS₃ limiting the overall current flowing through the device.

Typically, the diode photocurrent under forward bias is negligible in comparison to the reverse bias regime. While this is the case for $V_g > 0$, photocurrent generation in forward bias remarkably increases for $V_g < 0$ in our heterojunctions (Fig. 4b) and the external gate voltage can effectively switch the forward photocurrent generation on and off. Furthermore, for $V_g < 0$ and $V_{sd} > 0$, FePS₃/1L-MoS₂ photodiodes exhibit higher photocurrents than those obtained at zero and positive bias (Fig. 4b) and, thus, can operate as photodetectors both under reverse and forward configurations.

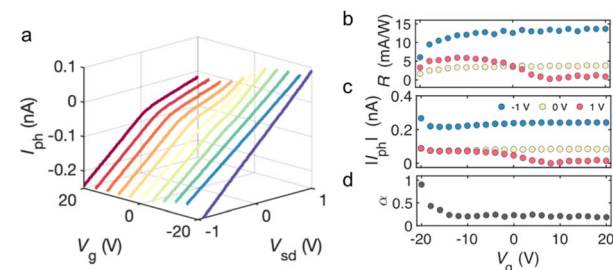


Fig. 4 (a) Photocurrent ($I_{\text{ph}} = I_{\text{light}} - I_{\text{dark}}$) as a function of V_{sd} and for different V_g , measured upon illumination with $\lambda = 532$ nm and $P_{\text{eff}} = 95$ nW for device B. (b) Responsivity as a function of applied gate voltage for negative, zero and positive bias voltage, obtained at $P_{\text{eff}} \sim 10$ nW. (c) Photocurrent as a function of V_g for negative, zero and positive bias voltage, and for $P_{\text{eff}} \sim 100$ nW. (d) Exponent α from photocurrent dependence on power ($I_{\text{ph}} = N \times P_{\text{eff}}^{\alpha}$), measured at $V_{\text{sd}} = 0$ V, within the power range where photo-gating effects dominate ($P_{\text{eff}} = 10\text{--}50$ nW).



In the case of higher incident powers ($P_{\text{eff}} \sim 100$ nW), I_{ph} behaves similarly to the low-power case within the range between $V_g = -10$ V to $+20$ V (Fig. 4c). However, an interesting change in this trend appears in Fig. 4c for $V_g < -10$ V, with a sudden increase of I_{ph} . To understand this behavior, we have analyzed the power law dependence of photocurrent on excitation power at zero bias and within the power range of 10 to 50 nW. In this regime, at $V_g = 0$ V, the photocurrent follows a power law expression, $I_{\text{ph}} = N \times P^\alpha$ with $\alpha < 1$ (Fig. 2c), indicating relevant contributions from photo-gating to photocurrent generation.⁵¹ Photo-gating effects have been extensively reported for both 1L-MoS₂ and FePS₃ due to the presence of charge-trap defects in both materials. Hence, the presence of photo-gating effects in the heterostructure is expected. For positive and small negative values of V_g , α exhibits values well below unity ($\alpha \ll 1$), suggesting that photo-gating effects strongly influence photocurrent generation (Fig. 4d). However, for $V_g < -10$ V, α increases significantly indicating that photo-gating effects cease to dominate the photocurrent generation at larger negative gate voltages. This occurs in the same range of values of V_g at which I_{ph} increases (Fig. 4c) and the forward conduction in dark is suppressed (Fig. 1g). Therefore, our results suggest that carrier depletion in 1L-MoS₂ entails a reduction in available trap states at the junction interface, resulting in improved photocurrent generation performance.

Conclusions

In summary, heterostructures built out from multilayer FePS₃ and single-layer MoS₂ (in short FePS₃/1L-MoS₂) constitute p-n photodiodes characterized by the coexistence of broadband electrical photo-response and robust excitonic emission. These unique features stem from the single-layer nature of MoS₂, the absorption properties of FePS₃, and the electronic properties of their interface. Compared to other devices containing single-layer TMDCs, FePS₃/1L-MoS₂ junctions present improved efficiency rates for UV photodetection. Moreover, both photocurrent and photoluminescence emission present a remarkable tunability under small, applied voltages, which likely arise from the band alignment at the interface. This exceptional tunability allows for precise control of the photoluminescence emission through minor adjustments to the voltage across the junction. Consequently, FePS₃/1L-MoS₂ heterostructures hold promise for gaining further insights into the competition between carrier dissociation and recombination at van der Waals interfaces, leading to the design of devices with enhanced performance. Furthermore, these heterostructures exemplify how varying alignments at different material interfaces can introduce additional functionality, tunability, and versatility to van der Waals devices.

Materials and methods

Crystal synthesis

Pristine FePS₃ crystals were grown *via* chemical vapor transport (CVT), using iodine as a transport agent,⁵² whereas bulk MoS₂ was provided commercially from SPI Supplies.

Heterostructure fabrication

Thin flakes of FePS₃ and MoS₂ were obtained through the Scotch tape method from their bulk crystals and transferred onto viscoelastic substrates, polydimethylsiloxane (PDMS), for optical inspection under a microscope. Once the ideal flakes were identified (proper thickness and geometry), the dry transfer method⁵³ was employed to stamp deterministically the desired flakes onto SiO₂/Si⁺⁺ (270 nm oxide layer) substrates with prepattern Ti/Au contacts. The mechanical exfoliation of FePS₃ crystals and the heterostructure stacking were carried out inside a glovebox inert Ar atmosphere. Single layer MoS₂ flakes were identified by micro-reflectance spectroscopy⁵⁴ and corroborated by Raman spectroscopy (Fig. S11†), using a Jasco NRS-5100 microscope. The thickness of the FePS₃ layer (40–60 nm) was determined by micro-reflectance spectroscopy⁵³ after device fabrication (see ESI Section S1†).

Micro-photoluminescence spectroscopy, three-terminal electrical measurements and scanning photocurrent map

The three types of experiments were carried out in a home-built equipment, provided of a confocal microscope and electrical contacts, to simultaneously study the interplay between photoluminescence and photoconductivity in the devices. Devices were mounted onto a motorized platform with movement along the x-y directions, allowing to run photocurrent maps with sub-micrometer step resolution. The excitation CW laser used for simultaneous photoluminescence and photocurrent measurements was a RLTMGL-532-500-1 (Roithner Lasertechnik), with an excitation line at 532 nm, fiber-coupled for a better integration in the setup. LED sources were used for other excitation wavelengths. For scanning photocurrent maps, a spot diameter of about 1 μm was used, whereas for opto-electronic transport measurements in Fig. 1, 2 and 4 a global illumination was employed (spot diameter ~80 μm). For photoluminescence spectra acquisition the excitation spot had ~8 μm of diameter and was centred on the vertical junction. Light emission was collected from a ~16 μm diameter spot. A Keithley 2450 sourcemeter was employed for the electrical measurements. Devices were kept in Ar atmosphere and characterized within an average time of 1–2 weeks, to avoid degradation upon air exposure.³³

Author contributions

Maria Ramos: device fabrication and characterization, data curation, formal analysis, visualization, writing – original draft. Marcos Gadea: device fabrication and characterization, data curation, formal analysis, writing – original draft. Samuel Mañas-Valero: material growth, device fabrication. Carla Boix-Constant: material growth, device fabrication. Eudomar Henríquez-Guerra: characterization. María Ángeles Díaz-García: validation, writing – review & editing. Eugenio Coronado: resources, validation, writing – review & editing. M. Reyes Calvo: conceptualization, formal analysis, funding acquisition, supervision, visualization, writing – original draft.



Conflicts of interest

There are no conflicts to declare.

Acknowledgements

The authors thank J. J. Baldoví and J. Canet-Ferrer for fruitful discussion. The authors acknowledge funding from Generalitat Valenciana through grants MFA/2022/045 and MFA/2022/050, IDIFEDER/2020/005, IDIFEDER/2021/016, PROMETEO Program and PO FEDER Program, the APOSTD/2020/249 fellowship for M. R., and support from the Plan Gen-T of Excellence for M. R. C. (CideGenT2018004); from the Spanish MCINN through grants PLASTOP PID2020-119124RB-I00, 2D-HETEROS PID2020-117152RB-100, and Excellence Unit “María de Maeztu” CEX2019-000919-M; and from the European Union (ERC AdG Mol-2D 788222).

References

- 1 D. A. Neamen, *Semiconductor Physics and Devices: Basic Principles*, McGraw-Hill, Boston, 3rd edn, 2003.
- 2 R. Frisenda, A. J. Molina-Mendoza, T. Mueller, A. Castellanos-Gomez and H. S. J. van der Zant, *Chem. Soc. Rev.*, 2018, **47**, 3339.
- 3 R. Liu, F. Wang, L. Liu, X. He, J. Chen, Y. Li and T. Zhai, *Small Struct.*, 2021, **2**, 2000136.
- 4 M. M. Furchi, A. Pospischil, F. Libisch, J. Burgdörfer and T. Mueller, *Nano Lett.*, 2014, **14**, 4785.
- 5 C. H. Lee, G. H. Lee, A. M. van der Zande, W. Chen, Y. Li, M. Han, X. Cui, G. Arefe, C. Nuckolls, T. F. Heinz, J. Guo, J. Hone and P. Kim, *Nat. Nanotechnol.*, 2014, **9**, 676.
- 6 A. Pospischil, M. M. Furchi and T. Mueller, *Nat. Nanotechnol.*, 2014, **9**, 257.
- 7 M. M. Furchi, F. Höller, L. Dobusch, D. K. Polyushkin, S. Schuler and T. Mueller, *npj 2D Mater. Appl.*, 2018, **2**, 3.
- 8 J. Wong, D. Jariwala, G. Tagliabue, K. Tat, A. R. Davoyan, M. C. Sherrott and H. A. Atwater, *ACS Nano*, 2017, **11**, 7230.
- 9 Y. Deng, Z. Luo, N. J. Conrad, H. Liu, Y. Gong, S. Najmaei, P. M. Ajayan, J. Lou, X. Xu and P. D. Ye, *ACS Nano*, 2014, **8**, 8292.
- 10 P. Wu, L. Ye, L. Tong, P. Wang, Y. Wang, H. Wang, H. Ge, Z. Wang, Y. Gu, K. Zhang, Y. Yu, M. Peng, F. Wang, M. Huang, P. Zhou and W. Hu, *Light: Sci. Appl.*, 2022, **11**, 6.
- 11 M. Long, E. Liu, P. Wang, A. Gao, H. Xia, W. Luo, B. Wang, J. Zeng, Y. Fu, K. Xu, W. Zhou, Y. Lv, S. Yao, M. Lu, Y. Chen, Z. Ni, Y. You, X. Zhang, S. Qin, Y. Shi, W. Hu, D. Xing and F. Miao, *Nano Lett.*, 2016, **16**, 2254.
- 12 K. Zhang, T. Zhang, G. Cheng, T. Li, S. Wang, W. Wei, X. Zhou, W. Yu, Y. Sun, P. Wang, D. Zhang, C. Zeng, X. Wang, W. Hu, H. J. Fan, G. Shen, X. Chen, X. Duan, K. Chang and N. Dai, *ACS Nano*, 2016, **10**, 3852.
- 13 X. Jiang, M. Zhang, L. Liu, X. Shi, Y. Yang, K. Zhang, H. Zhu, L. Chen, X. Liu, Q. Sun and D. W. Zhang, *Nanophotonics*, 2020, **9**, 2487.
- 14 J. Duan, P. Chava, M. Ghorbani-Asl, Y. Lu, D. Erb, L. Hu, A. Echresh, L. Rebohle, A. Erbe, A. V. Krasheninnikov, M. Helm, Y. J. Zeng, S. Zhou and S. Prucnal, *ACS Appl. Mater. Interfaces*, 2022, **14**, 11927.
- 15 Y. Wang, Y. Tang, H. Li, Z. Yang, Q. Zhang, Z. He, X. Huang, X. Wei, W. Tang, W. Huang and Z. Wu, *ACS Photonics*, 2021, **8**, 2256.
- 16 M. Long, Z. Shen, R. Wang, Q. Dong, Z. Liu, X. Hu, J. Hou, Y. Lu, F. Wang, D. Zhao, F. Ding, Y. Tu, T. Han, F. Li, Z. Zhang, X. Hou, S. Wang and L. Shan, *Adv. Funct. Mater.*, 2022, **32**, 2204230.
- 17 Y. Xin, X. Wang, Z. Chen, D. Weller, Y. Wang, L. Shi, X. Ma, C. Ding, W. Li, S. Guo and R. Liu, *ACS Appl. Mater. Interfaces*, 2020, **12**, 15406.
- 18 H. Gao, C. Du, J. Sun, J. Zhang, J. Leng, J. Li, W. Wang and K. Li, *Mater. Today Commun.*, 2023, **35**, 105959.
- 19 F. Withers, O. Del Pozo-Zamudio, A. Mishchenko, A. P. Rooney, A. Gholinia, K. Watanabe, T. Taniguchi, S. J. Haigh, A. K. Geim, A. I. Tartakovskii and K. S. Novoselov, *Nat. Mater.*, 2015, **14**, 301.
- 20 K. S. Novoselov, A. Mishchenko, A. Carvalho and A. H. Castro Neto, *Science*, 2016, **353**, aac9439.
- 21 J. Y. Lim, M. Kim, Y. Jeong, K. R. Ko, S. Yu, H. G. Shin, J. Y. Moon, Y. J. Choi, Y. Yi, T. Kim and S. Im, *npj 2D Mater. Appl.*, 2018, **2**, 1.
- 22 L. Gao, *Small*, 2017, **13**, 1603994.
- 23 T. U. Tran, D. A. Nguyen, N. T. Duong, D. Y. Park, D. H. Nguyen, P. H. Nguyen, C. Park, J. Lee, B. W. Ahn, H. Im, S. C. Lim and M. S. Jeong, *Appl. Mater. Today*, 2022, **26**, 101285.
- 24 T. Mueller and E. Malic, *npj 2D Mater. Appl.*, 2018, **2**, 29.
- 25 K. F. Mak, C. Lee, J. Hone, J. Shan and T. F. Heinz, *Phys. Rev. Lett.*, 2010, **105**, 136805.
- 26 A. Splendiani, L. Sun, Y. Zhang, T. Li, J. Kim, C. Y. Chim, G. Galli and F. Wang, *Nano Lett.*, 2010, **10**, 1271.
- 27 J. Yuan, S. Najmaei, Z. Zhang, J. Zhang, S. Lei, P. M. Ajayan, B. I. Yakobson and J. Lou, *ACS Nano*, 2015, **9**, 555.
- 28 Y. Wang, J. C. Kim, Y. Li, K. Y. Ma, S. Hong, M. Kim, H. S. Shin, H. Y. Jeong and M. Chhowalla, *Nature*, 2022, **610**, 61.
- 29 A. Zavabeti, P. Aukarasereenont, H. Tuohey, N. Syed, A. Jannat, A. Elbourne, K. A. Messalea, B. Y. Zhang, B. J. Murdoch, J. G. Partridge, M. Wurdack, D. L. Creedon, J. van Embden, K. Kalantar-Zadeh, S. P. Russo, C. F. McConville and T. Daeneke, *Nat. Electron.*, 2021, **4**, 277.
- 30 X. Zhang, H. Yu, W. Tang, X. Wei, L. Gao, M. Hong, Q. Liao, Z. Kang, Z. Zhang and Y. Zhang, *Adv. Mater.*, 2022, **34**, 2109521.
- 31 Y. Xiong, D. Xu, Y. Feng, G. Zhang, P. Lin and X. Chen, *Adv. Mater.*, 2023, **35**, 2206939.
- 32 Y. Gao, S. Lei, T. Kang, L. Fei, C. L. Mak, J. Yuan, M. Zhang, S. Li, Q. Bao, Z. Zeng, Z. Wang, H. Gu and K. Zhang, *Nanotechnology*, 2018, **29**, 244001.
- 33 M. Ramos, F. Carrascoso, R. Frisenda, P. Gant, S. Mañas-Valero, D. L. Esteras, J. J. Baldoví, E. Coronado, A. Castellanos-Gomez and M. R. Calvo, *npj 2D Mater. Appl.*, 2021, **5**, 1.
- 34 R. Brec, D. M. Schleich, G. Ouvrard, A. Louisy and J. Rouxel, *Inorg. Chem.*, 1979, **18**, 1814.



35 M. Ramos, F. Marques-Moros, D. L. Esteras, S. Mañas-Valero, E. Henríquez-Guerra, M. Gadea, J. J. Baldoví, J. Canet-Ferrer, E. Coronado and M. R. Calvo, *ACS Appl. Mater. Interfaces*, 2022, **14**, 33482.

36 M. Tamulewicz, J. Kutrowska-Girzycka, K. Gajewski, J. Serafińczuk, A. Sierakowski, J. Jadczak, L. Bryja and T. P. Gotszalk, *Nanotechnology*, 2019, **30**, 245708.

37 M. M. Furchi, D. K. Polyushkin, A. Pospischil and T. Mueller, *Nano Lett.*, 2014, **14**, 6165.

38 A. J. Molina-Mendoza, E. Giovanelli, W. S. Paz, M. A. Niño, J. O. Island, C. Evangelí, L. Aballe, M. Foerster, H. S. J. Van Der Zant, G. Rubio-Bollinger, N. Agraít, J. J. Palacios, E. M. Pérez and A. Castellanos-Gómez, *Nat. Commun.*, 2017, **8**, 14409.

39 X. Wang, L. Huang, Y. Peng, N. Huo, K. Wu, C. Xia, Z. Wei, S. Tongay and J. Li, *Nano Res.*, 2016, **9**, 507.

40 S. A. Svatek, E. Antolin, D. Y. Lin, R. Frisenda, C. Reuter, A. J. Molina-Mendoza, M. Muñoz, N. Agraít, T. S. Ko, D. P. De Lara and A. Castellanos-Gómez, *J. Mater. Chem. C*, 2017, **5**, 854.

41 W. Shockley and W. T. Read, *Phys. Rev.*, 1952, **87**, 835.

42 A. Castellanos-Gómez, J. Quereda, H. P. Meulen, H. P. van der Meulen, N. Agraít and G. Rubio-Bollinger, *Nanotechnology*, 2016, **27**, 115705.

43 R. Cheng, D. Li, H. Zhou, C. Wang, A. Yin, S. Jiang, Y. Liu, Y. Chen, Y. Huang and X. Duan, *Nano Lett.*, 2014, **14**, 5590.

44 J. Barnes, E. S. M. Tsui, K. W. J. Barnham, S. C. McFarlane, C. Button and J. S. Roberts, *J. Appl. Phys.*, 1997, **81**, 892.

45 S. J. Oh, J. Kim, J. M. Mativetsky, Y. L. Loo and C. R. Kagan, *ACS Appl. Mater. Interfaces*, 2016, **8**, 28743.

46 Y. Gong, J. Lin, X. Wang, G. Shi, S. Lei, Z. Lin, X. Zou, G. Ye, R. Vajtai, B. I. Yakobson, H. Terrones, M. Terrones, B. K. Tay, J. Lou, S. T. Pantelides, Z. Liu, W. Zhou and P. M. Ajayan, *Nat. Mater.*, 2014, **13**, 1135.

47 W. Yang, H. Kawai, M. Bosman, B. Tang, J. Chai, W. L. Tay, J. Yang, H. L. Seng, H. Zhu, H. Gong, H. Liu, K. E. J. Goh, S. Wang and D. Chi, *Nanoscale*, 2018, **10**, 22927.

48 X. Zhang, H. Nan, S. Xiao, X. Wan, Z. Ni, X. Gu and K. Ostrikov, *ACS Appl. Mater. Interfaces*, 2017, **9**, 42121.

49 X. Zong, H. Hu, G. Ouyang, J. Wang, R. Shi, L. Zhang, Q. Zeng, C. Zhu, S. Chen, C. Cheng, B. Wang, H. Zhang, Z. Liu, W. Huang, T. Wang, L. Wang and X. Chen, *Light: Sci. Appl.*, 2020, **9**, 114.

50 P. D. Cunningham, K. M. McCreary and B. T. Jonker, *J. Phys. Chem. Lett.*, 2016, **7**, 5242.

51 T. U. Tran, D. A. Nguyen, N. T. Duong, D. Y. Park, D. H. Nguyen, P. H. Nguyen, C. Park, J. Lee, B. W. Ahn, H. Im, S. C. Lim and M. S. Jeong, *Appl. Mater. Today*, 2022, **26**, 101285.

52 M. Šiškins, M. Lee, S. Mañas-Valero, E. Coronado, Y. M. Blanter, H. S. J. van der Zant and P. G. Steeneken, *Nat. Commun.*, 2020, **11**, 2698.

53 A. Castellanos-Gómez, M. Buscema, R. Molenaar, V. Singh, L. Janssen, H. S. J. van der Zant and G. A. Steele, *2D Mater.*, 2014, **1**, 011002.

54 R. Frisenda, Y. Niu, P. Gant, A. J. Molina-Mendoza, R. Schmidt, R. Bratschitsch, J. Liu, L. Fu, D. Dumcenco, A. Kis, D. P. D. Lara and A. Castellanos-Gómez, *J. Phys. D: Appl. Phys.*, 2017, **50**, 074002.

